The Astrophysical Journal, 931:144 (15pp), 2022 June 1 https://doi.org/10.3847/1538-4357/ac63b5

Unusually High HCO^+/CO Ratios in and outside Supernova Remnant W49B

Ping Zhou[1,2], Gao-Yuan Zhang[3], Xin Zhou[4], Maria Arias[5], Bon-Chul Koo[6], Jacco Vink[7,8,9], Zhi-Yu Zhang[1,2], Lei Sun[1,7], Fu-Jun Du[4], Hui Zhu[10], Yang Chen[1,2], Stefano Bovino[3], and Yong-Hyun Lee[11]
[1] School of Astronomy & Space Science, Nanjing University, 163 Xianlin Avenue, Nanjing 210023, People's Republic of China; pingzhou@nju.edu.cn
[2] Key Laboratory of Modern Astronomy and Astrophysics, Nanjing University, Ministry of Education, Nanjing 210023, People's Republic of China
[3] Departamento de Astronomía, Universidad de Concepción, Concepción, Chile; zgy0106@gmail.com
[4] Purple Mountain Observatory and Key Laboratory of Radio Astronomy, Chinese Academy of Sciences, 10 Yuanhua Road, Nanjing 210023, People's Republic of China
[5] Leiden Observatory, Leiden University, PO Box 9513, 2300 RA, Leiden, The Netherlands
[6] Department of Physics and Astronomy, Seoul National University, Seoul 08826, Republic of Korea
[7] Anton Pannekoek Institute for Astronomy, University of Amsterdam, Science Park 904, 1098 XH Amsterdam, The Netherlands
[8] GRAPPA, University of Amsterdam, Science Park 904, 1098 XH Amsterdam, The Netherlands
[9] SRON, Netherlands Institute for Space Research, Sorbonnelaan 2, 3584 CA Utrecht, The Netherlands
[10] Key Laboratory of Optical Astronomy, National Astronomical Observatories, Chinese Academy of Sciences, Beijing 100012, People's Republic of China
[11] Samsung SDS, Olympic-ro 35-gil 125, Seoul, Republic of Korea
Received 2021 December 7; revised 2022 March 23; accepted 2022 March 31; published 2022 June 3

Abstract

Galactic supernova remnants (SNRs) and their environments provide the nearest laboratories to study SN feedback. We performed molecular observations toward SNR W49B, the most luminous Galactic SNR in the X-ray band, aiming to explore signs of multiple feedback channels of SNRs on nearby molecular clouds (MCs). We found very broad HCO^+ lines with widths of $dv \sim 48$–75 km s^{-1} in the SNR southwest, providing strong evidence that W49B is perturbing MCs at a systemic velocity of $V_{\rm LSR} = 61$–65 km s^{-1}, and placing the W49B at a distance of 7.9 ± 0.6 kpc. We observed unusually high-intensity ratios of HCO^+ J=1–0/CO J=1–0 not only at shocked regions (1.1 ± 0.4 and 0.70 ± 0.16) but also in quiescent clouds over 1 pc away from the SNR's eastern boundary ($\geqslant$0.2). By comparing with the magnetohydrodynamics shock models, we interpret that the high ratio in the broad-line regions can result from a cosmic-ray (CR) induced chemistry in shocked MCs, where the CR ionization rate is enhanced to around 10–10^2 times of the Galactic level. The high HCO^+/CO ratio outside the SNR is probably caused by the radiation precursor, while the luminous X-ray emission of W49B can explain a few properties in this region. The above results provide observational evidence that SNRs can strongly influence the molecular chemistry in and outside the shock boundary via their shocks, CRs, and radiation. We propose that the HCO^+/CO ratio is a potentially useful tool to probe an SNR's multichannel influence on MCs.

Unified Astronomy Thesaurus concepts: Supernova remnants (1667); Molecular clouds (1072); Cosmic rays (329); X-ray sources (1822); Shocks (2086)

1. Introduction

Supernovae (SNe) are among the most energetic explosions in galaxies. SNe quickly fade away but leave their energy and metals in their supernova remnants (SNRs). While expanding in the interstellar medium (ISM), SNRs return a huge amount of energy (typically around the order of 10^{51} erg) to the galaxies via shocks, radiation, and cosmic rays (CRs; Vink 2020).

Theoretical studies show that SN feedback strongly regulates star formation and galaxy evolution (e.g., Scannapieco et al. 2008; Ostriker & Shetty 2011). Nevertheless, there are large uncertainties on the level of SN feedback, because it relies on the understanding of SN population and energy (Keller & Kruijssen 2022), and a clear knowledge of how multiple feedback channels (shocks, radiation, CRs) of SNR influence the ISM. Observing SNRs is a direct way to quantify the SN feedback and test those SN parameters applied in numerical simulations. For example, Koo et al. (2020) used H I and molecular observations of seven SNRs and found that their momentum and kinetic energy agree with those used in numerical simulations for typical SNe. In addition to the mechanical output, SNRs release part of their energy as CRs and radiation, which can influence the preshock area (see e.g., Vaupré et al. 2014).

As a relatively dense phase of the interstellar gas, molecular clouds (MCs) can efficiently slow down the SNR shocks, absorb the radiation, and interact with CRs. While shocks have been the most widely studied heating channel from SNRs, it is also crucial to learn the influence of SNRs' CRs and radiation. CRs are the main heating sources of dense molecular gas where UV emission is shielded (Goldsmith & Langer 1978). X-ray emission has been regarded as important ionization and heating source of neutral gas in active galactic nuclei (AGN) and primitive galaxies (Maloney et al. 1996; Lebouteiller et al. 2017; Vallini et al. 2019). The term X-ray dissociation regions or X-ray dominated regions (XDRs) has been used to describe the regions where the heating and chemistry of the gas are controlled mainly by the intense X-ray fluxes (Maloney et al. 1996). Due to the small cross section (decreasing with X-ray energy), the X-ray photons can traverse deep into the MCs and irradiate the gas opaque to UV photons. So far, more than 70 SNRs have been found to interact (or likely interact) with MCs (see Frail et al. 1996; Reach et al. 2006; Chen et al. 2014; Lee et al. 2019, and references therein). Many of them are bright in

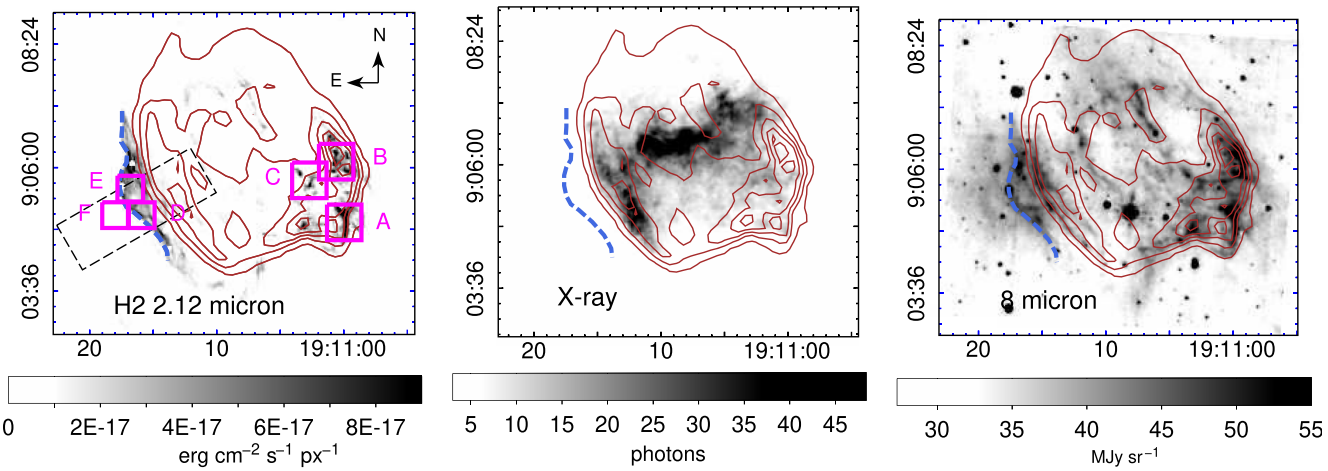

Figure 1. 2.12 μm H_2 (left panel, Lee et al. 2019), Chandra 0.3–10 keV X-ray photon image (middle panel; Zhou & Vink 2018), and Spitzer 8 μm image (right panel) of W49B with the VLA 327 MHz radio contours overlaid. The J2000 equatorial coordinates are used. The six square boxes in the first panel denote the regions for molecular line extraction as shown in Figure 2. The black, dashed region in the left panel is selected to compare brightness profiles of different wavelengths (see Figure 5). The blue, dashed curve in the SNR east delineates the eastern boundary of the H_2 filament.

the X-ray and γ-ray bands (Slane et al. 2015). They also have large infrared-to-X-ray flux ratios suggesting a radiative heating of dust (Koo et al. 2016). These SNRs and their environments provide the nearest laboratories to study the materials exposed to highly enhanced CRs and X-ray radiation.

SNR W49B is the most luminous Galactic SNR in the X-ray band (Immler & Kuntz 2005) and has been the subject of substantial X-ray studies on its plasma properties and SNR type (Hwang et al. 2000; Miceli et al. 2006; Keohane et al. 2007; Ozawa et al. 2009; Zhou et al. 2011; Lopez et al. 2013a, 2013b; Zhou & Vink 2018; Yamaguchi et al. 2018; Zhang et al. 2019; Sun & Chen 2020; Holland-Ashford et al. 2020; Siegel et al. 2020). W49B is detected in H.E.S.S. and Fermi-LAT observations, which suggest its GeV–TeV γ-ray emission is produced through the decay of π^0 created by the interaction between accelerated CR protons and nearby dense materials (H. E.S.S. Collaboration et al. 2018). Both the X-ray and γ-ray studies suggest that W49B is evolving in a dense medium. The IR study of W49B shows that the dense gas and dust have multiple temperature components and the SNR is evolving in a cloudy environment (Keohane et al. 2007; Zhu et al. 2014).

Although W49B appears to be a good target to study SNR feedback onto dense gas, there are disputes on the SNR's distance and associated clouds. Previous H I emission and absorption studies have not reached a consensus on the SNR distance issue. While some H I studies claimed that W49B lies 3–4 kpc closer than the star-forming region W49A to the west at ~11 kpc (Kazes 1970; Radhakrishnan et al. 1972; Zhang et al. 2013), others preferred a distance of 11–14 kpc (Lockhart & Goss 1978; Brogan & Troland 2001). The ^{12}CO observation shows a morphological relation between the molecular gas and the SNR at the local-standard-of-rest velocity ($V_{\rm LSR}$) at ~ 40 km s^{-1}, corresponding to a distance of 9–10 kpc (Chen et al. 2014; Zhu et al. 2014). The first kinetic evidence of W49B–MC association was provided by a recent study by Lee et al. (2020), who found that the near-infrared H_2 line centroid is at $V_{\rm LSR} = 64 \pm 2$ km s^{-1} and proposed an SNR distance of ~7.5 kpc. This velocity is consistent with those suggested by the earlier H I absorption studies (e.g., Kazes 1970) and radio recombination lines from ionized gas toward W49B (Downes & Wilson 1974; Liu et al. 2019). The dispute on W49B's distance is not ended. Recently, Sano et al. (2021) proposed a distance of 11 kpc for W49B using ^{12}CO observations, which reveal warm MCs at $V_{\rm LSR} \sim 10$ km s^{-1}.

Motivated by the above issues, we performed dedicated molecular observations toward W49B at the millimeter wavelength, aiming to achieve two goals: (1) to search for MCs perturbed by this SNR, and thus pin down the SNR distance; (2) more importantly, to explore signs of multiple feedback channels of an SNR on nearby MCs. We found unusually high HCO^+/CO ratios in and outside W49B, which are signs that the CRs, shocks, and radiation of W49B strongly influence the chemistry of the environmental gas. We present our observations and data in Section 2. The data analysis is shown in Section 3. Section 4 shows our interpretation of the unusual chemical properties, with discussions of relevant issues. The conclusion is summarized in Section 5.

2. Observation and Data

We performed millimeter observations toward W49B using the IRAM 30 m telescope during 2019 May 15–16 and 2020 July 24–27 (Project IDs: 167-18 and 024-20; PI: P. Zhou). We used the Eight MIxer Receiver (EMIR) to observe two frequencies (3 mm and 1 mm or 3 mm and 2 mm) simultaneously in the position-switching model. On-the-fly and on-off observing modes were applied for mapping and pointing observations, respectively. The back end of fast Fourier transform spectrometers (FTSs) provided a frequency resolution of 195 kHz, which corresponds to a velocity resolution of ~0.25 km s^{-1} at 235 GHz. The half-power beamwidth (HPBW) of the telescope was 10.″7 at 230 GHz, 20.″3 at 115 GHz, and 29″ at 86 GHz. The main-beam efficiencies at these three frequencies were 59%, 78%, and 81%, respectively.[12]

We mapped W49B in the frequency ranges 83.7–91.5 GHz, 109.5–117.3 GHz, and 225.1–236.0 GHz. The mapped region is similar to the field of view (FOV) of the multiband images in Figure 1. The observations are deeper in the east, west, and south regions to probe faint emission near the SNR boundary.

[12] http://www.iram.es/IRAMES/mainWiki/Iram30mEfficiencies

Table 1
Information for the IRAM 30 m Observation

Line	Frequency (GHz)	Image rms[a] (mK)
^{12}CO J=2–1	230.540	28–60
^{12}CO J=1–0	115.271	32–64
^{13}CO J=1–0	110.201	17–46
HNC J=1–0	90.664	10–34
HCO$^+$ J=1–0	89.189	12–39
HCN J=1–0	88.632	12–42

Note.
[a] The rms range of the data cube. The minimum rms is taken from the eastern and western regions of the SNRs.

In this paper, we focus on CO and HCO$^+$ lines, but we also detected a few other lines such as HCN and HNC lines. The line frequency and rms of a few molecular lines are tabulated in Table 1. All the IRAM 30 m data were reduced using the GILDAS software (vers. 10oct18[13]).

For comparison purposes, the data cubes of the HCO$^+$, ^{12}CO, ^{13}CO, and HCN emission were resampled to have the same velocity resolution of 0.7 km s^{-1}, while a larger velocity bin is sometimes used for broad lines to increase the signal-to-noise ratios. The pixel sizes of ^{12}CO J=2–1 and ^{12}CO/^{13}CO J=1–0 are 5″ and 10″, respectively. In the ratio maps, the ^{12}CO J=2–1 data are convolved to 30″ and regridded with a pixel size of 10″.

We also used multiwave band maps for comparison (see Figure 1). The VLA 327 MHz radio continuum emission data were adopted from Lacey et al. (2001). The 2.12 μm H_2 image from Lee et al. (2019) is reduced using the UKIRT Widefield Infrared Survey for H2 (UWISH2; Froebrich et al. 2011). The Chandra X-ray image in 0.3–10 keV was obtained from Zhou & Vink (2018) using the observations in 2000 (obs. ID: 117; PI: Stephen Holt) and 2011 (obs. IDs: 13440 and 13441; PI: Laura Lopez). We retrieved the 8 μm IR emission from the Galactic Legacy Infrared Midplane Survey Extraordinaire (GIMPSE; Churchwell et al. 2009) using the Spitzer telescope. The angular resolutions of the radio, H_2, X-ray, and 8 μm images are 6.″6 × 6.″2, 0.″7 (median seeing), 0.″5 (on-axis), and ∼2″, respectively (see aforementioned references for details of each image).

3. Results

3.1. Search for Shocked Molecular Gas

To search for MCs associated with W49B, we first investigated molecular line profiles across the SNR. Finding broadened molecular lines can provide strong evidence for a shock perturbation on the MCs (see e.g., Jiang et al. 2010), and also helps to determine the SNR distance.

We found very broad HCO$^+$ J=1–0 emission only in the southwestern regions of W49B at $V_{\rm LSR}$ = 40–150 km s^{-1} (see the spectra in Figure 2. All the regions correspond to strong H_2 emission in the southwest (see the box regions A, B, and C in Figure 1).

By fitting the broad lines with Gaussian profiles, we obtained line widths (FWHM) of 48 ± 3 km s^{-1}, 62 ± 3 km s^{-1}, and 75 ± 7 km s^{-1} at regions A, B, and C, respectively (see Table 2). These lines are too broad to be attributed to quiescent gas but are strong evidence of MCs accelerated by the SNR shock. The line widths are also distinctly larger than those predicted in C-type shock, where the H_2 molecules survive up to a shock velocity of 45 km s^{-1} (Draine et al. 1983). At region C, only one prominent narrow HCO$^+$ line is seen at $V_{\rm LSR}$ ∼ 61 km s^{-1}, while the faint line at $V_{\rm LSR}$ ∼ 10 km s^{-1} is too far away from the broad component to be related. There are also narrow HCO$^+$ lines at $V_{\rm LSR}$ = 61–63 km s^{-1} at regions A and B, and at $V_{\rm LSR}$ = 64–65 km s^{-1} at regions D–F (see further discussions in Section 3.2.1 and Section 4). We fitted the narrow HCO$^+$ lines with $V_{\rm LSR}$ > 60 km s^{-1} using Gaussian lines and tabulate the fit results in Table 2.

Our study supports an SNR systemic velocity of $V_{\rm LSR}$ = 61–65 km s^{-1}, where we found narrow lines (2–6 km s^{-1} for HCO$^+$ emission based on the Gaussian fit; Table 2) nearest to the broad emission and with relatively high HCO$^+$/CO intensity ratios. The systemic velocity is consistent with that obtained from the previous H_2 spectral study (64 ± 2 km s^{-1}; Lee et al. 2020). These narrow line components can be explained as the preshock gas. This LSR velocity, combined with the measured Galactic rotation curve (Reid et al. 2014), places W49B at a far distance of 7.9 ± 0.6 kpc or a near distance of 4.1 ± 0.6 kpc, where the uncertainty is given at the 1σ level based on the Monte Carlo method by Wenger et al. (2018).[14] Due to the H I absorption up to $V_{\rm LSR}$ = 70 km s^{-1} (the LSR velocity of the tangent point at ∼6 kpc; see e.g., Zhu et al. 2014), W49B should be a bright radio source behind the tangent point. Therefore, W49B is located at a distance of 7.9 ± 0.6 kpc. This means that W49B is far away from the star-forming region W49A at a distance of $11.1^{+0.8}_{-0.7}$ kpc (based on parallax measurements using H_2O masers; Zhang et al. 2013).

A centroid shift of the HCO$^+$ broad line is clearly seen from regions A to C, indicating different viewing angles to the shock. The shift reaches the maximum of ∼36 km s^{-1} at region C. In regions B and C, we only found redshift HCO$^+$ line wings, corresponding to the receding gas that is shocked on the far side of the SNR. The MCs at region A are shocked perpendicular to the line of sight, as its HCO$^+$ profile shows both redshift and blueshift wings, and the broad-line centroid is the same as the systemic velocity. An interaction with dense MCs explains the deformed radio morphology in the southwest. The schematic views of clouds A–F from the observer and the western side are given in Figure 9 in the Appendix.

Figure 3 shows the spatial distribution of shocked HCO$^+$ in the velocity range $V_{\rm LSR}$ = 70–120 km s^{-1}. This velocity range corresponds to the red wing of broadened lines. We have not found any broad HCO$^+$ or ^{12}CO lines in other regions of the SNR, except for those visible in Figure 3. This means that the kinetic evidence of SNR–MC interaction has only been established in the southwestern regions of W49B. The distribution of ^{12}CO J=2–1 and HCO$^+$ J=1–0 in the velocity range $V_{\rm LSR}$ = 0–80 km s^{-1} with a step of 5 km s^{-1} are shown in Figures 10 and 11, respectively, in the Appendix.

3.2. Molecular Emission at the Systemic Velocity

3.2.1. HCO$^+$ and ^{12}CO Emission

As the distance of W49B has been determined, we study the properties of the neighboring MCs. Figure 4 shows the distribution of HCO$^+$ J=1–0, ^{12}CO J=1–0, ^{12}CO J=2–1, and HCO$^+$/^{12}CO J=1–0 ratio at around the systemic velocity of the

[13] http://www.iram.fr/IRAMFR/GILDAS/

[14] https://www.treywenger.com/kd

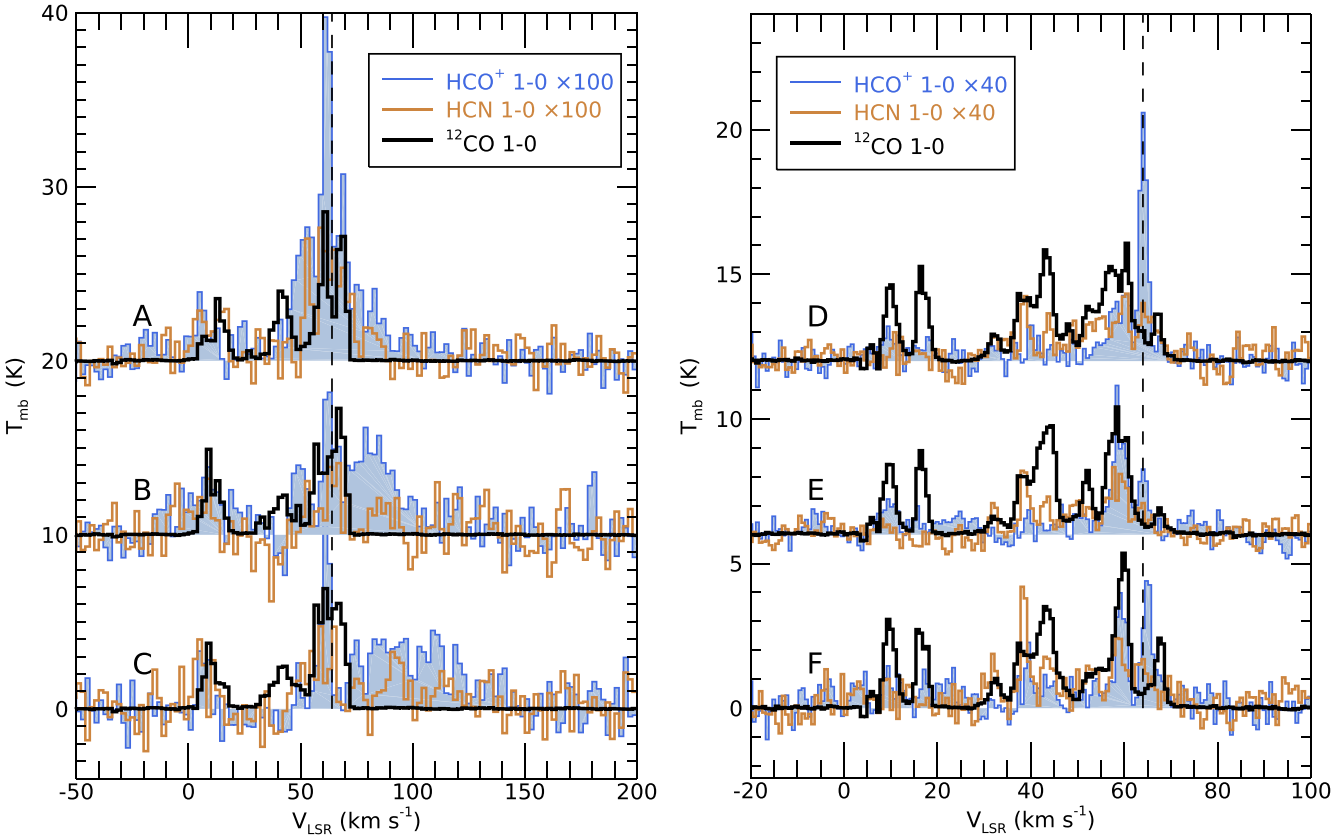

Figure 2. Spectra of ^{12}CO and scaled HCO$^+$ and HCN at six regions labeled in Figure 1. The dashed vertical line indicates the LSR velocity of 64 km s^{-1}, where a high HCO$^+$/CO line ratio is found outside the SNR. All data were convolved to reach the same beam size of 30″.

SNR. Although HCO$^+$ and ^{12}CO emissions are found in the interior of W49B, they might arise from background or foreground MCs, given the lack of physical evidence for an association with the SNR. Only the southwestern region has been found to show broadened HCO$^+$ emission (see Section 3.1).

It is of interest to learn whether SNRs can influence the ISM outside its radio boundary and how the influence is reflected in the chemistry of the MCs. We found enhanced HCO$^+$/^{12}CO $J=$ 1–0 ratios near the eastern H_2 filament, and two clouds in the northeastern and southwestern regions, while the ratio is $\lesssim 10^{-2}$ in the SNR interior. Hereafter we focus on the 2.12 μm H_2 filament 0.′5 ($\sim$1.2 pc) away from the eastern radio boundary of W49B (see Figure 1 and Keohane et al. 2007).[15] The near-IR H_2 emission requires hot or irradiated molecular gas in a high excitation state, raising questions about the heating mechanism of this filament (see discussions in Keohane et al. 2007; Lee et al. 2020).

To test whether the gas at the eastern 2.12 μm H_2 filament is shock heated, we extracted HCO$^+$ J=1–0 spectra at regions D, E, and F. The line centroid of the 2.12 μm H_2 emission is at $V_{\rm LSR} = 64.3$–65.5 km s^{-1} (Lee et al. 2020). At similar velocities, we found HCO$^+$ lines with narrow line widths ($\Delta v = 2$–4 km s^{-1}), which argues against shock perturbation for producing the HCO$^+$ emission. The narrow line width is not unexpected, since the SNR's forward shock as traced by the radio emission does not reach the H_2 filament and thus should not directly impact the molecular gas. Another HCO$^+$ peak is found at $V_{\rm LSR} \sim 58$ km s^{-1} to the SNR east (regions D, E, and F). There is no clear evidence to support an association between this velocity and the SNR, given the normal HCO$^+$/^{12}CO line ratio ($\sim$0.02) and line widths.

The eastern HCO$^+$ gas with an unusually high HCO$^+$/^{12}CO ratio extends even further away from the SNR than the H_2 filament, although an HCO$^+$ knot is seen between the filament and the SNR radio boundary. The ^{12}CO $J=2$–1 map with a better angular resolution also shows a filamentary structure east of the H_2 filament. The layered distributions of different molecular emissions can be more clearly seen in Figure 5, which is cut along a slice across the eastern SNR shell (see the black dashed box in Figure 1). Both HCO$^+$ and H_2 emission peaks lie $\gtrsim$50″ (1.9 pc) away from the radio peak. The H_2 emission is sharply enhanced on the western surface of the HCO$^+$ emission, while the ^{12}CO $J=1$–0 profile has little resemblance with the H_2 profile. In Section 4.3.3, we will discuss how the distribution is explained by the irradiated gas.

3.2.2. HCN Lines and Other Molecular Lines

We found HCN J=1–0 emission toward W49B, which contains a hyperfine triplet due to the nuclear quadrupole moment of N ($F=2$–1, $F=1$–1, $F=0$–1). The separation of the hyperfine lines between highest and lowest frequencies is 3.522 MHz, which corresponds to 11.8 km s^{-1}. The brightness pattern among the hyperfine structures is not constant but

[15] Enhanced HCO$^+$/^{12}CO intensity ratios are found in two clouds in the northeast and southwest of W49B. The two clouds are warmer than 20 K and have the largest column densities in the FOV. Our observations cannot tell whether the two clouds are physically associated with the SNR or unassociated star-forming regions, and thus we do not discuss these clouds. Moreover, given that the ^{12}CO emission is optically thick, a high HCO$^+$/CO intensity ratio does not necessarily mean a high abundance ratio.

Table 2
Parameters of the HCO^+ and HCN Emission in Six Regions

Region[a]	HCO^+ (1-0)				HCN (1-0)
	Gaussian Fit[b]				
	V_{LSR} (km s^{-1})	Δv (km s^{-1})	T_{peak} (K)	$\int T_{mb} dv$ (K km s^{-1})[c]	$\int T_{mb} dv$ (K km s^{-1})[c]
A (broad)	61.8 ± 0.8	47.5 ± 2.9	0.064 ± 0.005	3.07 ± 0.17	1.60 ± 0.15
(narrow)	61.9 ± 0.1	5.7 ± 0.4	0.14 ± 0.1		
(narrow)	69.3 ± 0.2	2.8 ± 0.7	0.06 ± 0.01		
B (broad)	77.3 ± 0.9	61.7 ± 3.0	$0.044 \pm 0.0.002$	2.33 ± 0.13	0.88 ± 0.23
(narrow)	62.6 ± 0.2	5.2 ± 0.7	0.061 ± 0.006		
C (broad)	97.8 ± 1.9	75.3 ± 6.5	0.035 ± 0.002	2.45 ± 0.19	1.03 ± 0.19
(narrow)	61.4 ± 0.1	5.0 ± 0.4	0.13 ± 0.01		
D	63.8 ± 0.3	2.4 ± 0.1	0.192 ± 0.008	1.00 ± 0.10	1.05 ± 0.10
E	63.8 ± 0.2	3.6 ± 0.6	0.054 ± 0.007	0.82 ± 0.13	0.75 ± 0.09
F	64.7 ± 0.1	3.7 ± 0.3	0.11 ± 0.01	1.31 ± 0.12	1.20 ± 0.21

Notes.
[a] The selected regions are displayed in the upper-left panel of Figure 1, with the HCO^+ and HCN spectra shown in Figure 2.
[b] The HCO^+ line centroid, FWHM line width, and peak brightness fitted using one (D–F) or more Gaussian lines (A–C). Only line components with $V_{LSR} > 60$ km s^{-1} are fitted. The HCO^+ spectrum is composed of a "broad" and one or two "narrow" components at regions A, B, or C, but only one narrow line at regions D, E, or F.
[c] HCO^+ or HCN intensity integrated for all line components in the range of $V_{LSR} = 40$–150 km s^{-1}.

depends on the excitation condition (e.g., Walmsley et al. 1982; Loughnane et al. 2012).

Due to the difficulty of separating hyperfine structures, we only examine the HCN properties of the six regions where enhanced HCO^+ are shown (see regions in Figure 1). We integrated the HCN J=1–0 emission at $V_{LSR} = 40$–150 km s^{-1} and tabulated the values of the six regions in Table 2. The flux ratio of HCO^+/HCN is 1.9–2.6 in the shocked gas and ∼1 near the eastern H_2 filament.

The enhancement of HCO^+/HCN J=1–0 flux at the shocked regions is an intriguing phenomenon, which was also found in SNR IC 443 (with a ratio of ∼3, Denoyer & Frerking 1981). The explanation of the enhancement requires further investigation, which is outside the scope of this paper.

We also detected HNC J=1–0 at ∼ 64 km s^{-1} at regions A–F. SiO J=2–1 and DCO^+ J=2–1 lines are not detected in our observations.

4. Discussion

4.1. Large HCO^+/CO Ratios in W49B

4.1.1. Observed Intensity Ratios

We found large HCO^+/CO intensity ratios of 0.2–1 in both the shock-broadened lines in the southwest and narrow lines outside the SNR eastern boundary (see Figure 2), while the typical intensity ratios in other molecular components along the line of sight are $\lesssim 10^{-2}$. This is observational evidence to support that SNRs can influence the chemistry not only of the shocked clouds but also of MCs that are over 1 pc far away.

In the shocked regions, the HCO^+/CO intensity is enhanced at the broadened line wings. In the velocity range of 75–150 km s^{-1} (without strong narrow ^{12}CO lines), the integrated HCO^+ intensities are 0.66 ± 0.14, 1.28 ± 0.11, and 1.74 ± 0.16 K km s^{-1}, respectively, at regions A, B, and C, while the values for ^{12}CO J=1–0 lines are 0.49 ± 0.33, 1.84 ± 0.40, and 1.55 ± 0.31 K km s^{-1}, respectively. The ^{12}CO emission has only a 4–5σ detection at regions B and C. One cannot claim detection of broad ^{12}CO emission in region A as it is below 2σ, We estimate the flux ratio of $I(HCO^+)/I(CO) = 1.1 \pm 0.4$ at region C and 0.70 ± 0.16 at region B. Given the large velocity gradient, it is reasonable to assume the optically thin case for the HCO^+ and ^{12}CO emission in the broad lines.

Near the eastern H_2 filament, the line ratio of HCO^+/CO is large at $V_{LSR} \sim 64$ km s^{-1} compared to those at other velocities. At region D, the main-beam temperatures of HCO^+ and ^{12}CO are 0.22 K and $\leqslant$1.0 K, respectively, corresponding to an $HCO^+/^{12}CO$ intensity ratio $\geqslant$0.2. Here the ^{12}CO J=1–0 main-beam temperature is regarded as an upper

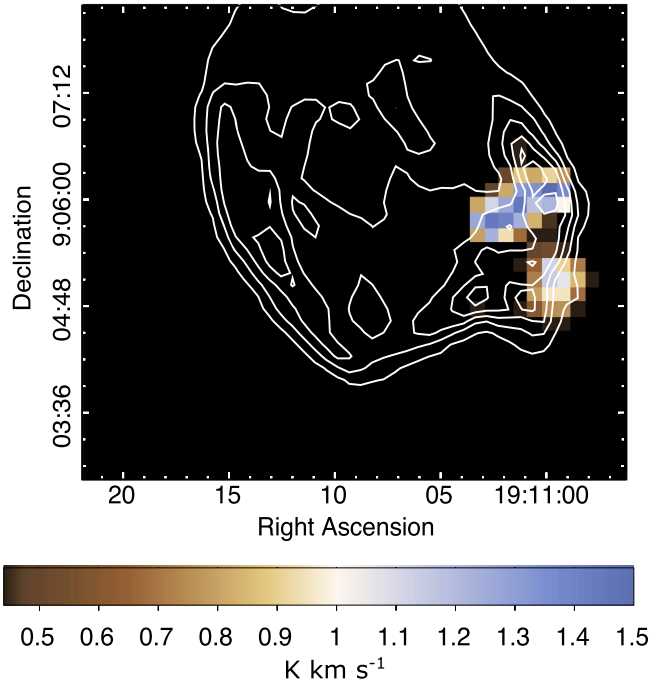

Figure 3. Distribution of the shocked HCO^+ gas in the velocity range $V_{LSR} = 70$ km s^{-1} to 120 km s^{-1}, overlaid with the 327 MHz radio contours. Values with $\geqslant 5\sigma$ detection are shown.

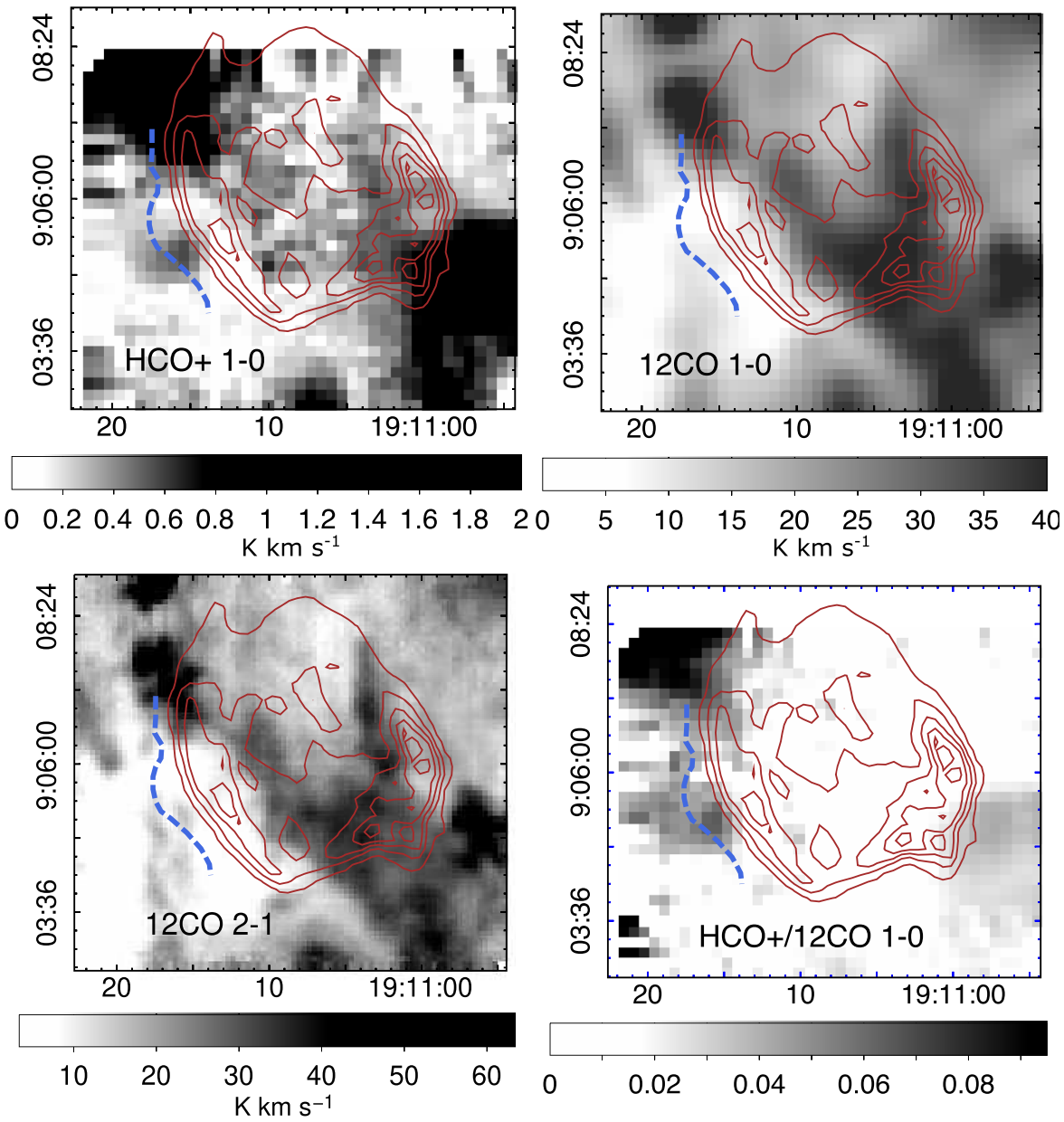

Figure 4. HCO^+ J=1–0, ^{12}CO J=1–0, ^{12}CO J=2–1, and $HCO^+/^{12}CO$ J=1–0 images toward W49B in V_{LSR} = 61–67 km s^{-1} with the VLA 327 MHz radio contours overlaid (J2000 equatorial coordinates). The blue, dashed curve in the SNR east delineates the eastern boundary of the H_2 filament.

limit, as it is in a line valley and the emission is contaminated by the red wing of the unassociated component at $V_{LSR} \sim 58$ km s^{-1}. The ^{12}CO J=1–0 emission is probably optically thin, as indicated by a large ^{12}CO J=2–1/J=1–0 $\sim$1.5 (only $\lesssim 1$ in the optically thick case in the local thermodynamic equilibrium case; see Zhou et al. 2018).

The HCO^+/CO intensities obtained above are subsequently used to estimate the abundance ratios (see Section 4.1.2), which will be further compared with those predicted by the thermochemical models of molecular gas in the SNR environment (see Section 4.2).

4.1.2. Column Densities and Abundance Ratios

On the assumption of local thermodynamic equilibrium (LTE) and optically thin emission, the HCO^+ J = 1–0 line can be used to estimate the column density N(HCO^+) (Mangum & Shirley 2015):

$$N(\mathrm{HCO^+}) \approx 2.46 \times 10^{11} \frac{(T_{ex} + 0.78)\exp\left(\frac{h\nu}{kT_{ex}}\right)}{\exp\left(\frac{h\nu}{kT_{ex}}\right) - 1} \times \frac{\int T_{mb}(\mathrm{HCO^+})dv\,(\mathrm{km\ s^{-1}})}{J_\nu(T_{ex}) - J_\nu(T_{bg})}\ \mathrm{cm^{-2}} \quad (1)$$

where h and k are Planck constant and Boltzmann constant, respectively, ν is the frequency of the J = 1–0 transition, $J(T) = \frac{h\nu}{\exp(h\nu/kT) - 1}$, and the Cosmic Microwave Background temperature T_{bg} = 2.73 K. For a kinetic/excitation temperature

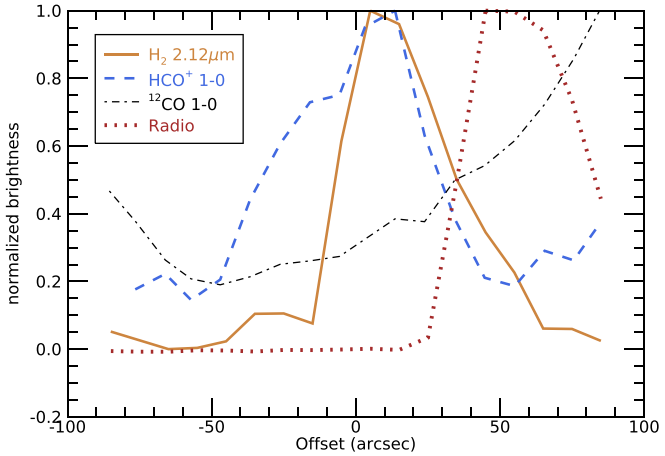

Figure 5. Brightness distribution of H_2 2.12 μm, HCO^+, and ^{12}CO, and 327 MHz radio emission cut across the SNR eastern shell from the east to the west (angle = 30°; see the region in Figure 1).

$T_{ex} \gg T_{bg}$, the above equation is simplified as

$$N(\mathrm{HCO^+}) \sim 5.7 \times 10^{10} T_{ex} \exp\left(\frac{4.28}{T_{ex}}\right) \times \int T_{mb}(\mathrm{HCO^+}) dv (\mathrm{km\ s^{-1}})\ \mathrm{cm^{-2}}. \quad (2)$$

Similarly, we derive the ^{12}CO column density using the optically thin ^{12}CO $J = 1$–0 emission for $T_{ex} \gg T_{bg}$:

$$N(\mathrm{CO}) \sim 4.32 \times 10^{13} T_{ex} \exp\left(\frac{5.53}{T_{ex}}\right) \times \int T_{mb}(\mathrm{CO}) dv (\mathrm{km\ s^{-1}})\ \mathrm{cm^{-2}}. \quad (3)$$

From Equations (2) and (3), it is convenient to obtain $N(\mathrm{HCO^+})/N(\mathrm{CO}) \sim 1.3 \times 10^{-3} I(\mathrm{HCO^+})/I(\mathrm{CO}) \sim 1.3 \times 10^{-3} T_{mb}(\mathrm{HCO^+})/T_{mb}(\mathrm{CO})$ for a gas excitation temperature $T_{ex} \gtrsim 20$ K.

We estimate the abundance ratio $X(\mathrm{HCO^+})/X(\mathrm{CO}) = N(\mathrm{HCO^+})/N(\mathrm{CO}) = 3 \times 10^{-4}$–$2 \times 10^{-3}$ at the regions with enhanced $\mathrm{HCO^+}$/CO intensity ratios. The abundance ratios are significantly larger than those found in cold MCs (10^{-6}–10^{-4}), where the fractional abundance of CO relative to H_2 ($X(\mathrm{CO}) \sim 10^{-4}$, Dickman 1978; Lucas & Liszt 1998) is a few orders of magnitude larger than that of $\mathrm{HCO^+}$($X(\mathrm{HCO^+}) \sim 10^{-10}$–$10^{-8}$ (varies with excitation conditions; Miettinen 2014; Fuente et al. 2019).

We caution that the $\mathrm{HCO^+}$/CO abundance ratios are obtained by assuming an LTE condition, considering we only have one $\mathrm{HCO^+}$ transition. Further observations with mid-J and high-J transitions of $\mathrm{HCO^+}$ and ^{12}CO are needed for a precise diagnosis of the excitation conditions.

4.2. Model the Chemical and Physical Properties of a Shocked MC Exposed to CRs

The SNR shock can heat and ionize the gas and change the abundance of molecular species. The GeV–TeV observations of W49B have proved that the SNR is accelerating CR protons (H.E.S.S. Collaboration et al. 2018), which are known as important sources regulating molecular chemistry. We used two codes to compute the $\mathrm{HCO^+}$/CO abundance ratios of a shocked MC exposed to CRs.

4.2.1. Constant-temperature Chemical Model

We first used a chemical network with molecules containing H, C, O, and N (Bovino et al. 2016; Hily-Blant et al. 2018; Le Gal et al. 2014) to simulate the chemical evolution in a shock-heated cloud by employing the astrochemistry package KROME (Grassi et al. 2014). The initial condition is assumed to be in equilibrium at a temperature $T = 15$ K for various densities. We then calculate the evolution of every species after an abrupt increase of the temperature to about 10^2 K, 10^3 K, and 10^4 K (corresponding to a shock velocity of about 1.4 km s^{-1}, 5 km s^{-1}, and 15 km s^{-1}, respectively; see Figure 6). In the upper row of Figure 6, we ignored the effect of photoionization. In the lower panels, we used an extinction level, $A_V = 1$, with a standard Drain UV field (Draine 1978). The exact radiation field and extinction near W49B have been thus far unclear (see Section 4.3.3). By setting a moderate extinction level A_V to 1, we assume the column density for shielding the radiation field is about 1.9×10^{21} cm^{-2} (Bohlin et al. 1978) to show the effect of a moderate UV photoionization condition. We set a lower limit of the molecular number density, 10^{-8} cm^{-3}, to make sure that the molecular emission is observable and prevent a small denominator.

According to our network, at the temperature of 10^3 K, the main channels to produce $\mathrm{HCO^+}$ are $\mathrm{CO + H_3^+ \rightarrow HCO^+ + H_2}$ and $\mathrm{HOC^+ + H_2 \rightarrow HCO^+ + H_2}$. The former reaction converts some CO molecules to $\mathrm{HCO^+}$, raising the abundance ratio between $\mathrm{HCO^+}$ and CO. Figure 6 reveals a higher $\mathrm{HCO^+}$/CO ratio for enhanced CRs, which can increase the number of ions in the MCs. When the temperature is raised to 10^4 K, both CO and $\mathrm{HCO^+}$ molecules can be easily dissociated, but the CR ionization reaction chain (such as the reaction $\mathrm{HCO} \xrightarrow{\mathrm{CR}} \mathrm{HCO^+} + e^-$ and $\mathrm{CO + H_3^+ \rightarrow HCO^+ + H_2}$) keeps the $\mathrm{HCO^+}$ dropping slower than CO, resulting in an $\mathrm{HCO^+}$/CO abundance ratio $> 10^{-3}$. In a slow shock with a lower temperature of 10^2 K, the $\mathrm{HCO^+}$/CO abundance ratios are below 10^{-3} for various densities. Although the CR reaction chain still produces $\mathrm{HCO^+}$, the recombining reaction of $\mathrm{HCO^+}$ (e.g., $\mathrm{HCO^+ + e^- \rightarrow CO + H}$) and the reactions between $\mathrm{HCO^+}$ and neutral atoms or molecules (e.g., $\mathrm{HCO^+ + C \rightarrow CO + CH^+}$) are relatively fast in this low temperature, resulting in a low $\mathrm{HCO^+}$/CO abundance ratio.

We note that this constant-temperature model is a simplified model that does not include cooling/heating mechanisms or magnetic fields, and the chemical network only contains up to four atom molecules. Nevertheless, this model shows that $\mathrm{HCO^+}$/CO abundances are highly sensitive to gas physical condition and CR ionization rate. This model is also useful to learn the main channels to form $\mathrm{HCO^+}$ in a given condition.

4.2.2. MHD Shock Model

We further simulated the $\mathrm{HCO^+}$/CO ratio in a magnetohydrodynamic (MHD) shock using the Paris–Durham shock code (Godard et al. 2019), which takes the influence of magnetic fields on shocks into account. The MHD shock code calculates the physical and chemical evolution of the gas, by including over 125 species linked by more than 1000 reactions and with cooling and heating processes considered. We considered a plane-parallel shock wave propagating in a molecular and dusty homogeneous medium with a magnetic field strength of $B = \left(\frac{n_H}{\mathrm{cm^{-3}}}\right)^{1/2} \mu$G, where n_H is the preshock gas density of the three-phase gas $n_H = n(\mathrm{H}) + 2n(\mathrm{H_2}) + n(\mathrm{H^+})$.

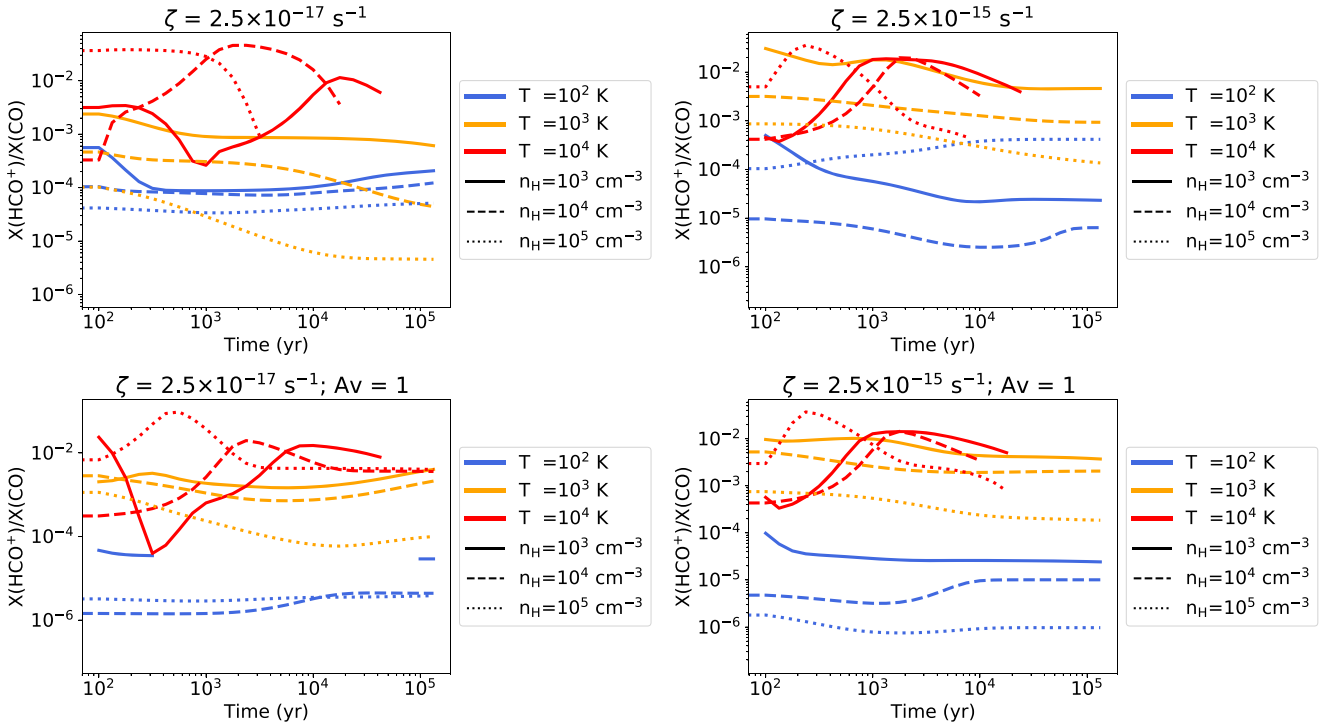

Figure 6. The chemical evolution in the shocked molecular region. ζ is the CR ionization rate per H_2. The number density of hydrogen n_H is contributed by atoms, ions, and molecules. A_v is the extinction magnitude of the standard Draine UV photon field to which the MC is exposed. In the upper row, the effect of the UV photon field is assumed to be extremely small. We discard the ratio values when either the number density of HCO^+ or CO is lower than 10^{-8} cm^{-3}.

First, we calculated the thermochemical conditions of the preshock gas, adopting the standard initial distribution of elemental fractional abundances among gas-phase species, PAHs, icy grain mantles, and grain cores, as adopted by Flower & Pineau des Forêts (2003). We allow the gas to evolve in a quiet and dark condition with given densities and the Galactic level CR ionization rate per H_2 $\zeta = 2.5 \times 10^{-17}$ s^{-1} (a few 10^{-17} s^{-1} in dense MCs; van der Tak & van Dishoeck 2000). The final static thermochemical properties are used as input parameters for the preshock gas.

Subsequently, we run the MHD shock models, which cover entrance shock velocities of 5–50 km s^{-1} (a step of 5 km s^{-1}), and preshock densities of 10^3, 10^4, and 10^5 cm^{-3}. The Galactic level ($\zeta = 2.5 \times 10^{-17}$ s^{-1}) and higher levels ($\zeta = 2.5 \times 10^{-16}$ s^{-1}, $\zeta = 2.5 \times 10^{-15}$ s^{-1}) of CR ionization rates are considered to evaluate the CRs' influence. We adopted a shock timescale of 1 kyr in MCs. With an age of 5–6 kyr (Zhou & Vink 2018; Sun & Chen 2020), W49B should not have spent its whole lifetime interacting with MCs. Moreover, the molecular shock timescale is consistent with the recombination age of the cooler X-ray plasma in the southwestern region of W49B (~1 kyr; Holland-Ashford et al. 2020), where the thermal conduction with the cold and dense gas likely caused a rapid cooling of the X-ray-emitting plasma.

The simulations show that the shock types at $V_{sh} < 20$ km s^{-1} are nonstationary "continuous" shocks (young C-type shock), which are composed of a magnetic precursor and J-type tail (see Lesaffre et al. 2004, for the temporal evolution of young C-type shocks). The shocks at $V_{sh} \gtrsim 20$ km s^{-1} become "jump" shocks (J-type), where the ions and neutrals are coupled.

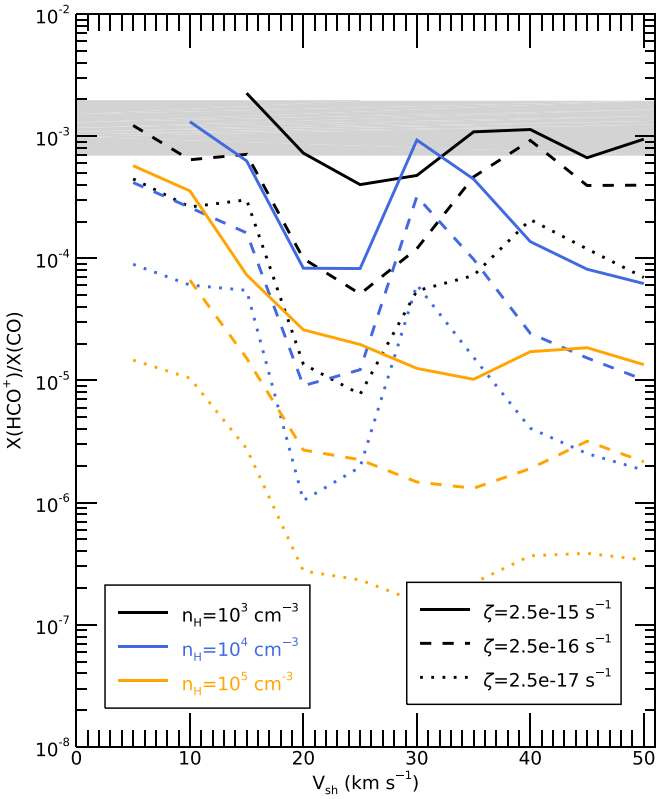

Figure 7. The abundance ratio of HCO^+/CO as a function of entrance shock velocity, preshock gas density n_H, and CR ionization rate per H_2 ζ in the MHD shock models. The shock age is taken as 1 kyr. The observed values in regions B and C are denoted by the gray area.

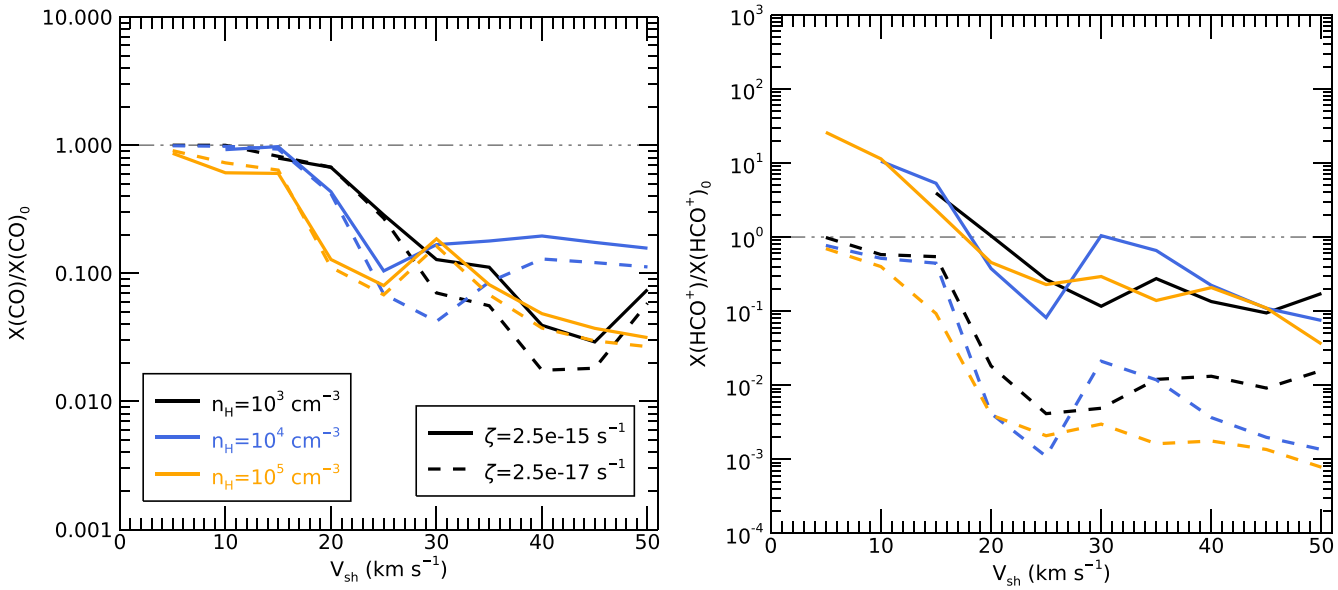

Figure 8. The abundance ratio of ^{12}CO (left) and HCO$^+$ (right) relative to those in the preshock gas for a shock age of 1 kyr.

Figure 7 shows the modeled abundance HCO$^+$/CO ratios with a shock age of 1 kyr, as a function of shock velocity, preshock gas density, and cosmic-ray ionization rate. The abundance ratio is obtained from the integrated HCO$^+$ and ^{12}CO column densities in the shocked layer. X(HCO$^+$)/X(CO) tends to decrease with increasing preshock gas density and shock velocity, while the enhanced CR ionization rate can significantly increase the ratio.

A high CR ionization and a moderate density are needed to explain the observed large X(HCO$^+$)/X(CO), while the Galactic level CR (dotted lines) and very dense preshock gas (orange color) cases predict a too-low value. It is reasonable to expect two orders of magnitude higher CR ionization rate ζ near W49B, as found in other middle-age SNRs such as IC443 ($\zeta = 2 \times 10^{-15}$ s^{-1}; Indriolo et al. 2010) and W28 (Vaupré et al. 2014). With $\zeta = 2.5 \times 10^{-15}$ s^{-1}, the high X(HCO$^+$)/X(CO) can be reached in a wide range of shock velocities (see Figure 7). At $V_{\rm sh} \geqslant 25$ km s^{-1}, X(HCO$^+$)/X(CO) is less sensitive to the shock velocity but relies more on the CR ionization rate and density.

The broad HCO$^+$ lines ($\Delta v = 50$–75 km s^{-1}) found in W49B hint at a fast shock in the MC. The broad-line profile can be explained by either a single cloud with a large velocity dispersion or multiple shocked structures accelerated to different LSR velocities. In either case, a large shock velocity is needed to explain the large line centroid shifts (from $V_{\rm LSR} \sim 60$ km s^{-1} of the quiescent gas to $V_{\rm LSR} \sim 100$ km s^{-1} for gas in region C).

We suggest that the high HCO$^+$/CO ratio in the broad-line regions can result from a CR-induced chemistry in shocked MCs with a preshock density $n_{\rm H} \sim 10^3$–10^4 cm^{-3}. An enhancement of the HCO$^+$/CO ratio induced by CRs has also been found in a low-to-intermediate density cloud, IC 348 (Luo et al. 2022, in preparation). We do not claim an enhancement of the HCO$^+$ abundance, but only an enhancement of the HCO$^+$/CO abundance ratio. Our MHD shock modeling shows that the ^{12}CO molecules tend to be dissociated with enhanced shock velocities. ^{12}CO abundance can be 1–2 orders of magnitude lower than the level in the preshock gas with $V_{\rm sh} \gtrsim 20$ km s^{-1} (see Figure 8). The HCO$^+$ abundance also presents a negative trend to the shock velocity, but the high-level CR ionization strongly regulates the HCO$^+$ chemistry and maintains it above 0.1 of the preshock level. When shock velocity is low ($V_{\rm sh} \lesssim 15$ km s^{-1}) and does not effectively destroy HCO$^+$ molecules, the enhanced CRs can indeed cause an HCO$^+$ abundance enhancement. Nevertheless, the low shock velocities are unlikely to explain the broad HCO$^+$ profiles and the weak CO emission. Therefore, the observed high ratio of HCO$^+$/CO does not mean an enhancement of HCO$^+$ but reflects the more efficient destruction of CO molecules than that of the HCO$^+$ in the faster shock.

There are a few caveats in our MHD modeling and comparison. We have not evaluated the influence of external radiation on the HCO$^+$/CO abundance ratio, but only show that the enhanced CRs can already explain the observation. The UV spectrum of W49B is unclear, while the X-ray-induced physics/chemistry is not considered in the MHD models. Moreover, the observed X(HCO$^+$)/X(CO) for comparison is calculated under a simplified LTE assumption.

4.3. Irradiated Gas in the SNR East

An unusually high HCO$^+$/CO line ratio is also found over 1 pc away from the SNR eastern boundary (see Figure 2). Here we discuss three types of precursors that might cause peculiar chemical properties to the MCs ahead of the shock (near the eastern H$_2$ filament; see Figure 1): (1) CR precursor, (2) magnetic precursor, and (3) radiation precursor. We do not consider the SNR blast wave as the direct source, as it is too far from these regions to cause the HCO$^+$/CO enhancement. The narrow HCO$^+$ line widths do not suggest the shock perturbation, either.

4.3.1. CR Precursor

CRs can diffuse away from the SNR boundary. The diffusion length of CRs is expressed as (see Vink 2012, and references therein):

$$l_{\rm diff} = 1.0 \times 10^{-2}\ {\rm pc}\ \ \eta^{1/2} \left(\frac{E}{1\ {\rm GeV}}\right)^{1/2} \left(\frac{B}{10\ \mu{\rm G}}\right)^{-1/2} \left(\frac{t}{5\ {\rm kyr}}\right)^{1/2} \quad (4)$$

where η accounts for the deviation from Bohm diffusion ($\lesssim$10 in young SNRs, Vink 2012), E is the CR particle energy, B is

the magnetic field and t is the acceleration age, equal to the SNR age (5–6 kyr).

Low-energy CRs (<1 GeV) cannot diffuse over 1 pc away from the shock, unless η is unusually large. High-energy cosmic rays with $E \geqslant 1$ TeV could reach this distance, but their energy losses via pion production are a few orders of magnitude larger than ionization losses, meaning inefficient in MC heating (Mannheim & Schlickeiser 1994). Assuming a hadronic origin of the γ-ray emission from W49B, γ-rays carry about at least $1/3$ of the pion production losses, and the spectrum peaks at about $1/10$ of the energy of the primary CRs (Hinton & Hofmann 2009). The total γ-ray flux of W49B above 0.1 TeV is $F(>0.1\,\mathrm{TeV}) \sim 4 \times 10^{-12}\,\mathrm{erg\,cm^{-2}\,s^{-1}}$ (H.E.S.S. Collaboration et al. 2018), only comparable to the flux of the 2.12 μm H_2 line east to the SNR ($F(2.12\,\mu\mathrm{m\,H_2}) \sim 5 \times 10^{-12}\,\mathrm{erg\,cm^{-2}\,s^{-1}}$; Lee et al. 2019). The comparison suggests that the ionization losses from TeV CRs of W49B are insufficient to power the observed molecular emissions. Therefore, CRs are not the favored heating source for the clouds east to W49B.

4.3.2. Magnetic Precursor

A magnetic precursor can appear in weakly ionized MCs, which coexist two distinct fluids in the shocks: a neutral fluid and an ionized fluid. If the magnetosonic speed exceeds the shock speed ($V_m > V_{\rm sh}$), compressive waves can be generated upstream ahead of the shock. The extent of the magnetic precursor for a stationary C-type shock is expressed as (Draine 2011):

$$l_{\rm mag} \approx 3.4 \times 10^{15}\ \mathrm{cm}\left(\frac{B}{10\,\mu\mathrm{G}}\right)^{2}\left(\frac{V_{\rm sh}}{10\ \mathrm{km\,s^{-1}}}\right)^{-1} \times \left(\frac{n_{\rm H}}{10^{2}\ \mathrm{cm^{-3}}}\right)^{-2}\left(\frac{x_i}{10^{-4}}\right)^{-1} \quad (5)$$

where the fractional ionization x_i is $\sim 10^{-4}$ in the diffuse MCs. For a dark cloud with a density of 10^2–10^5 cm^{-3}, there is a simple approximation $x_i \approx 10^{-5}(n_{\rm H}/\mathrm{cm^{-3}})^{-1/2}$ (Draine 2011). The ionization fraction is raised in clouds exposed to enhanced UV/X-ray radiation or CRs, which could happen near W49B. Assuming the magnetic energy conservation, the magnetic field in the cloud is estimated as $B = b_0(n_{\rm H}/\,\mathrm{cm^{-3}})^{1/2}\mu$G. Equation (5) is then rewritten as $l_{\rm mag} \sim 3.4 \times 10^{19}$ cm $b_0^2[(n_{\rm H}/\,\mathrm{cm^{-3}})(V_{\rm sh}/\,\mathrm{km\,s^{-1}})^2]^{-1/2}$. A previous X-ray study found a blast wave velocity of $V_{\rm bw} \sim 480\ \mathrm{km\,s^{-1}}$ in W49B, with a preshock intercloud density of $n_0 \sim 10\ \mathrm{cm^{-3}}$ (Zhou & Vink 2018). Assuming a pressure equilibrium between the blast wave and cloud shock $n_{\rm H}V_{\rm sh}^2 \sim n_0 V_{\rm bw}^2$ (McKee & Cowie 1975), the expression of the magnetic precursor length for W49B can be simplified as: $l_{\rm mag} \sim 2 \times 10^{16} b_0^2$ cm, where b_0 is in the level of $\sim$1 in typical MCs (Crutcher et al. 2010) but could vary with specific environments. It was proposed that the magnetic precursor causes the high-excitation H_2 emission outside the SNR boundary (Keohane et al. 2007). However, our calculation suggests that the magnetic precursor length of W49B is too small to excite the H_2 and HCO^+ emission 1 pc away from the SNR boundary, while W49B is unlikely to be located in a strongly magnetized medium (Brogan & Troland 2001).

Our MHD models reveal that shock types in the southwestern MCs are not stationary C-type shocks but are likely J-type with shock velocities $\gtrsim$20 km s^{-1} (see Section 4.2.2). As the ions and neutrals are coupled in the J-type shocks, the magnetic precursor can be ignored.

4.3.3. Radiation Precursor

Unlike the CR and magnetic precursors that have short-length scales, radiation can freely escape the SNR until the photons are absorbed/scattered by the ISM. W49B is the most luminous Galactic SNR in the X-ray band (Immler & Kuntz 2005) with an intrinsic luminosity of $L_{\rm X} \sim 2$–$9 \times 10^{38} d_8^2$ erg s^{-1} in the 0.3–10 keV band (the upper limited is recalculated using the XMM-Newton data and model in Sun & Chen 2020), where the uncertainty mainly comes from different absorption models. Its soft X-ray emission is so heavily absorbed that the observed 0.3–10 keV X-ray luminosity is only 5×10^{35} erg s^{-1}. This means that most of the soft X-ray energy is transferred to the environment of W49B and the ISM along the line of sight.

Previous X-ray spectroscopy reveals that the soft X-ray emission below 1 keV is contributed by hot plasmas with a temperature of $kT \sim 0.2$–0.3 keV ($\sim 3 \times 10^6$ K Zhou & Vink 2018; Holland-Ashford et al. 2020; Sun & Chen 2020). If the soft X-ray emission is characterized by an *apec* model with a temperature of 0.177 keV and a normalization of 86.7 cm^{-5} (see the best-fit *apec* + 2∗*vvrnei* model in Sun & Chen 2020), we can roughly estimate a UV luminosity of $L_{\rm UV} \sim 6 \times 10^{39}$ erg s^{-1} at 6–300 eV and 7×10^{37} erg s^{-1} at 6–13.6 eV. The values are likely lower limits, as there could be undetected gas components cooler than $\sim$0.2 keV. Therefore, W49B is also a luminous UV source.

Given the high X-ray and UV luminosity of W49B, we suggest radiation precursor be a plausible source for the hot MCs to the SNR east. As the UV emission is highly absorbed, we do not clearly know the UV spectrum of W49B and thus do not evaluate its influence on the MCs outside W49B. However, the strong UV emission can explain the existence of strong 8 μm IR emission to the SNR east (see Figure 1), which traces either the polycyclic aromatic hydrocarbons (PAHs) in strong radiation fields or hot dust grains (Draine 2011). There is a good correlation between the near-IR H_2 emission and 8 μm emission, but the latter emission is even more extended (up to 1.′7 or 4 pc) from the radio boundary.

The large X-ray luminosity of W49B makes it a potential laboratory to study MCs in XDRs. It has been proposed that the intense X-ray emission from SNRs could transfer a fraction of their energy to MCs and give rise to strong vibration-rotational H_2 (Draine & Woods 1990, 1991). Indeed, W49B is the most luminous SNRs in both the X-ray band and near-IR H_2 emission based on our current knowledge (Lee et al. 2019). According to XDR models by Maloney et al. (1996), the H_2 emission in XDRs has a relatively low ratio H_2 2–1 $S(1)$/ 1–0 $S(1)$ $\sim$0.1 ($\lesssim$0.3), similar to the values in shock excited gas, while the mean ratio for UV fluorescent excitation of H_2 is $\sim$0.5–0.6 (Black & van Dishoeck 1987). Lee et al. (2020) observed a ratio of 0.07–0.10 in the eastern H_2 filament and proposed that the gas could be either shocked or X-ray-irradiated gas. Here we prefer the latter scenario, as the former case is less likely.

We found that the HCO^+ emission is generally in the outer layer of the H_2 filament to the SNR east (see Figure 5). This distribution can also be explained with XDR models, which predict that H_2 emission arises from the surface layer of the

irradiated MCs (Maloney et al. 1996). The layered HCO^+ and H_2 distribution likely reflects a radiation attenuation into the MCs. The XDR models by Meijerink & Spaans (2005) indeed provide multiple solutions for producing the observed high HCO^+/CO intensity ratio ($\geqslant$0.2 to the SNR east). However, the X-ray spectral shape ($\exp(-E/1\ \mathrm{keV})$) and flux range (1.6, 16, and 160 erg cm^{-2} s^{-1}) in the available XDR models do not cover that in W49B (see the X-ray spectral models in, e.g., Sun & Chen 2020), while the observed molecular transitions are too few to constrain the gas excitation condition. A reliable comparison can be provided in the future using new molecular observations and XDR models with flexible X-ray spectral parameters.

4.4. Remarks about HCO^+/CO Ratios near SNRs

In W49B, optically thin HCO^+ emission and HCO^+/CO ratio are strongly enhanced in the shocked regions and thus appear to be good tracers of SNR shock under these particular conditions. We also note that high HCO^+/CO intensity ratios of $\sim$1 are found in the shocked gas in IC 443 (Dickinson et al. 1980; Dickman et al. 1992). It is of interest to explore the HCO^+/CO ratios in more SNRs that are impacting MCs, to test whether the high HCO^+/CO ratio can be a good tracer of SNR shock in various physical conditions. If it is the case, HCO^+ lines will be a useful tool to identify new SNR–MC associations on the Galactic plane.

Broadened ^{12}CO emission has been widely used to probe shocked MCs and many known SNR–MC interaction has been identified in this way (Jiang et al. 2010). However, ^{12}CO emission is not a shock tracer, but is usually used as a molecular gas tracer since CO is an abundant molecule in the interstellar MCs and is easy to be excited. In the $V_{\rm LSR}$ range of 0–80 km s^{-1}, the ^{12}CO $J=1$–0 and $J=2$–1 emissions toward W49B are subject to the severe line crowding, because multiple quiescent MCs lie along the line of sight. This causes problems to discern any broad profiles. Although the line-of-sight contamination should be free at $V_{\rm LSR} > 80$ km s^{-1} (see Figure 2), we still do not detect strong broad ^{12}CO emission across the SNR, probably because of the efficient destruction of ^{12}CO molecules in the shocks (see Figure 8).

Finally, we observed a high HCO^+/CO intensity ratio outside W49B, which is likely due to the strong X-ray/UV radiation. It is also of interest to test whether such high ratios can be found outside other SNRs (or other X-ray/UV luminous sources) in the molecular environment. Nevertheless, the ratio should be subject to multiple physical parameters (such as temperature, density, and optical depth), in addition to radiation fields. Further modelings of the MC chemistry in strong radiation are needed for comparison.

5. Conclusion

We have performed a molecular line survey toward SNR W49B using the IRAM 30 m telescope. In this paper, we focus on HCO^+ and ^{12}CO emissions to probe the influence of SNR on the MCs through shocks, CRs, and radiation. Our main conclusions are as follows:

1. W49B is interacting with MCs in its southwest, where we found very broad HCO^+ emissions with widths of 48–75 km s^{-1}. The observed flux ratios of HCO^+/CO in two shocked regions are 1.1 ± 0.4 and 0.70 ± 0.16, which are significantly larger than that in typical MCs. In the LTE condition and optically thin case, the abundance ratios are estimated as $X(HCO^+)/X(CO) = 7\times10^{-4}$–$2\times10^{-3}$. We have also found an enhanced flux ratio of HCO^+/HCN of 1.9–2.6 in the shocked gas, larger than the ratio of $\sim$1 near the eastern H_2 filament.
2. By comparing with the MHD shock models, we suggest that the high HCO^+/CO ratio in the broad-line regions can result from a CR-induced chemistry in shocked MCs, where the CR ionization rate is enhanced to 1–2 orders of magnitude larger than the Galactic level. The observed high HCO^+/CO ratio in the broad lines does not mean an enhancement of HCO^+ but reflects a stronger decline of the CO abundance than that of HCO^+.
3. Our molecular study supports the systemic velocity of W49B is $V_{\rm LSR}\sim61$–65 km s^{-1} and the distance is 7.9 ± 0.6 kpc, consistent with that obtained using the near-IR H_2 emission (Lee et al. 2020). Therefore, W49B does not have a physical relation to the star-forming region W49A.
4. SNR W49B also influences the molecular chemistry far ahead of its shocks. We have found an unusually high HCO^+/CO intensity ratio ($\geqslant$0.2) over 1 pc east of the SNR's radio boundary, where the ^{12}CO emission is optically thin. The HCO^+ lines outside the SNR are narrow ($dV=2$–4 km s^{-1}), disfavoring an SNR shock perturbation. The characteristic lengths of low-energy CRs and magnetic precursors of W49B are much smaller than 1 pc, and thus are unlikely to cause the enhanced ratio while the radiation precursor (X-ray or UV) is capable to change the molecular chemistry outside the SNR.
5. As the most luminous Galactic SNR in the X-ray band, W49B is a potential laboratory to study the XDRs. The XDR models can explain the low H_2 2–1 $S(1)$/1–0 $S(1)$ $\sim$0.1 ratio in the H_2 filament east to the SNR (Lee et al. 2020), while PDR models predict larger values. Moreover, we found that the HCO^+ structure is east of the H_2 filament. This layered distribution can be explained under XDR models, which predict that H_2 emission arises from the surface layer of the irradiated MCs. The layered HCO^+ and H_2 distribution likely reflect a radiation attenuation into the MCs. Although some XDR models can explain the observed HCO^+/CO ratio, we caution that future models and observations are needed for a reliable comparison.
6. The HCO^+/CO ratio is a potentially useful tool to study the influence of SNR shocks, CRs, and radiation on the MC chemistry. The low-J ^{12}CO emission alone does not seem to be a good probe for shock conditions near W49B on the Galactic plane, as it is weak in the shocked gas, but too strong in unassociated clouds along the line of sight.

The authors are thankful to the anonymous referee for constructive suggestions. We also thank Xiao Zhang for the helpful discussion about the γ-ray emission of W49B. This work is based on observations carried out under project numbers 167-18 and 024-20 with the IRAM 30 m telescope. IRAM is supported by INSU/CNRS (France), MPG (Germany), and IGN (Spain). Shock models published in this paper have been produced with the Paris–Durham shock code (Flower & Pineau des Forêts 2003; Lesaffre et al. 2013; Godard et al. 2019, http://ism.obspm.fr). P.Z. acknowledges the

support from NSFC grant No. 11590781, Nederlandse Organisatie voor Wetenschappelijk Onderzoek (NWO) Veni Fellowship, grant no. 639.041.647, and the Nederlandse Onderzoekschool Voor Astronomie (NOVA). M.A. thanks the NWO for support via the Talent Programme Veni grant. The work of B.-C.K is supported by Basic Science Research Program through the National Research Foundation of Korea funded by the Ministry of Science, ICT and Future Planning (2020R1A2B5B01001994). Z.-Y.Z. acknowledges the support of NSFC (grants 12041305, 12173016) and the Program for Innovative Talents and Entrepreneurs in Jiangsu. Y.C. thanks the support of NSFC grants 11773014, 11633007, and 11851305.

Software: GILDAS (Pety 2005; Gildas Team 2013), DS9 (Joye & Mandel 2003; Smithsonian Astrophysical Observatory 2000), XSPEC (vers. 12.9.0u, Arnaud 1996).

Appendix

To illustrate the distributions of the six regions A–F near W49B, we provide the schematic view in Figure 9. It shows that regions B and C are located in the back side of W49B, while regions D–F are not contacted by the SNR shock. From the western side view, regions A, B, and C are in the front.

Figures 10 and 11 show the distribution of ^{12}CO J=2–1 and HCO^+ J=1–0 near W49B in the velocity range V_{LSR} = 0–80 km s^{-1} with a step of 5 km s^{-1}.

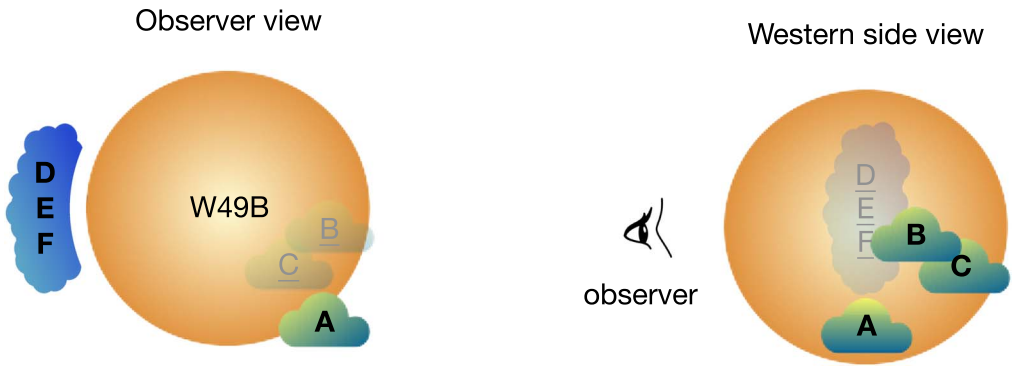

Figure 9. Schematic view of the interpreted positions of the six regions A–F denoted in Figure 1. The underlined letters denote the regions behind W49B through the observer view or western side view.

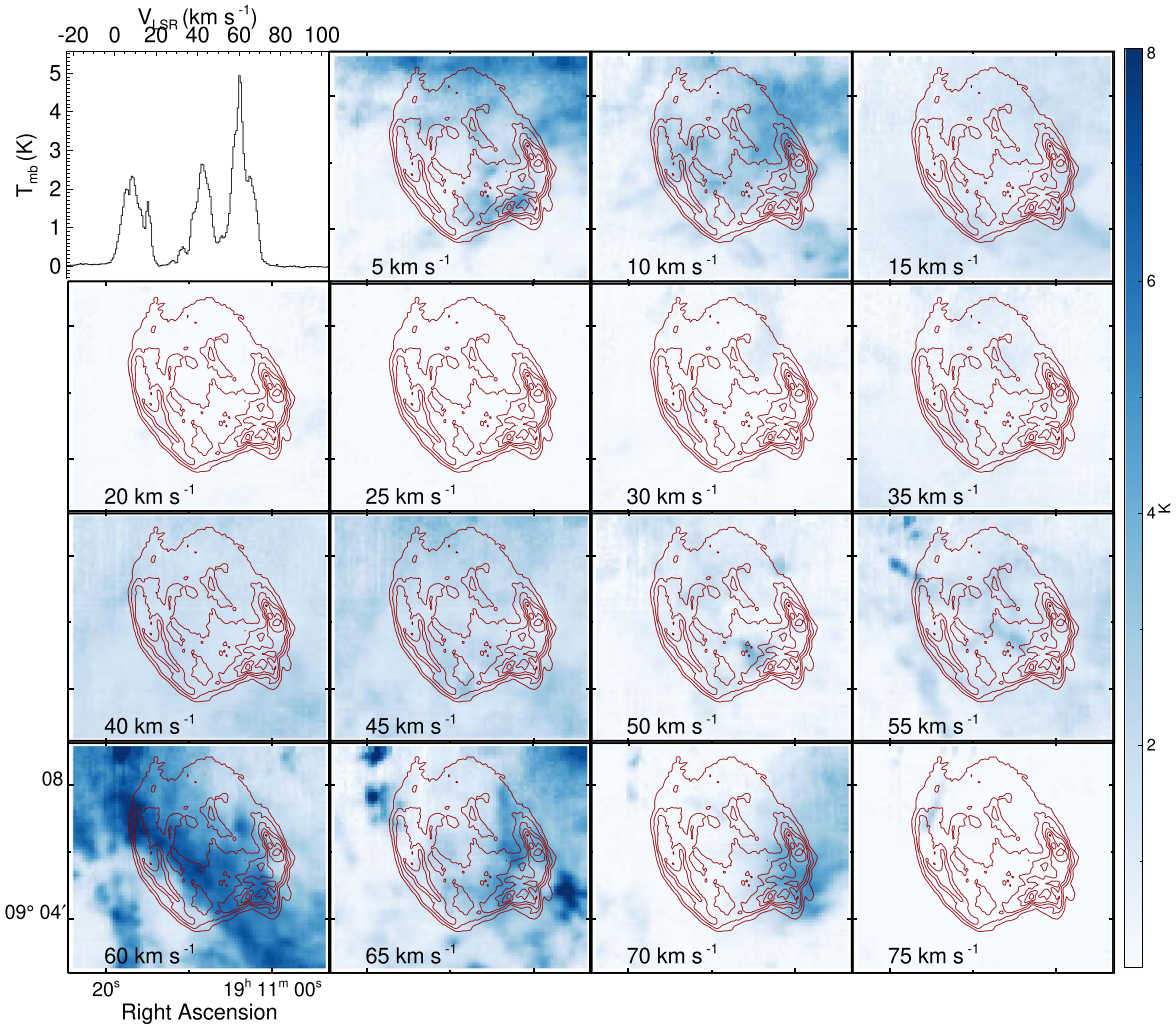

Figure 10. Channel map of the averaged main-beam temperature of ^{12}CO $J = 2$–1 emission with a step of 5 km s^{-1}, overlaid with contours of 327 MHz radio emission. The same contours are used for the maps in the rest of the paper. The top left panel shows the spectrum averaged over the FOV.

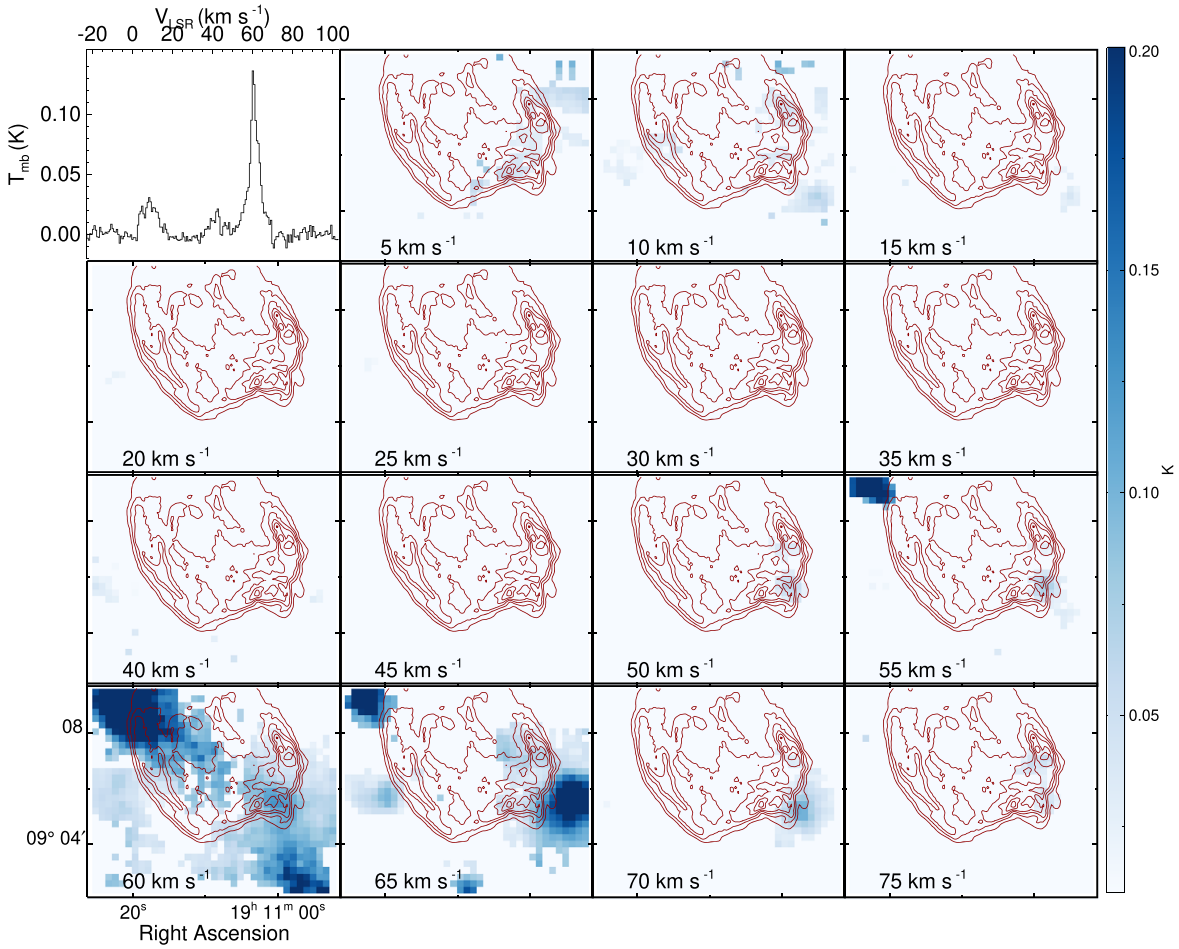

Figure 11. Channel map of the averaged main-beam temperature of HCO^+ $J = 1$–0 emission with a step of 5 km s^{-1}, overlaid with contours of 327 MHz radio emission. The top left panel shows the spectrum averaged over the FOV. Pixels with over 5σ HCO^+ line detection are displayed.

ORCID iDs

Ping Zhou https://orcid.org/0000-0002-5683-822X
Xin Zhou https://orcid.org/0000-0003-2418-3350
Maria Arias https://orcid.org/0000-0002-7918-904X
Bon-Chul Koo https://orcid.org/0000-0002-2755-1879
Jacco Vink https://orcid.org/0000-0002-4708-4219
Zhi-Yu Zhang https://orcid.org/0000-0002-7299-2876
Lei Sun https://orcid.org/0000-0001-9671-905X
Fu-Jun Du https://orcid.org/0000-0002-7489-0179
Hui Zhu https://orcid.org/0000-0003-3775-3770
Yang Chen https://orcid.org/0000-0002-4753-2798
Stefano Bovino https://orcid.org/0000-0003-2814-6688
Yong-Hyun Lee https://orcid.org/0000-0003-3277-2147

References

Arnaud, K. A. 1996, in ASP Conf. Ser. 101, Astronomical Data Analysis Software and Systems V, ed. G. H. Jacoby & J. Barnes (San Francisco, CA: ASP), 17
Black, J. H., & van Dishoeck, E. F. 1987, ApJ, 322, 412
Bohlin, R. C., Savage, B. D., & Drake, J. F. 1978, ApJ, 224, 132
Bovino, S., Grassi, T., Capelo, P. R., Schleicher, D. R. G., & Banerjee, R. 2016, A&A, 590, A15
Brogan, C. L., & Troland, T. H. 2001, ApJ, 550, 799
Chen, Y., Jiang, B., Zhou, P., et al. 2014, in IAU Symp. 296, Supernova Environmental Impacts, ed. A. Ray & R. A. McCray (Cambridge: Cambridge Univ. Press), 170
Churchwell, E., Babler, B. L., Meade, M. R., et al. 2009, PASP, 121, 213
Crutcher, R. M., Wandelt, B., Heiles, C., Falgarone, E., & Troland, T. H. 2010, ApJ, 725, 466
Denoyer, L. K., & Frerking, M. A. 1981, ApJL, 246, L37
Dickinson, D. F., Rodriguez Kuiper, E. N., Dinger, A. S. C., & Kuiper, T. B. H. 1980, ApJL, 237, L43
Dickman, R. L. 1978, ApJS, 37, 407
Dickman, R. L., Snell, R. L., Ziurys, L. M., & Huang, Y.-L. 1992, ApJ, 400, 203
Downes, D., & Wilson, T. L. 1974, A&A, 34, 133
Draine, B. T. 1978, ApJS, 36, 595
Draine, B. T. 2011, Physics of the Interstellar and Intergalactic Medium (Princeton, NJ: Princeton Univ. Press)
Draine, B. T., Roberge, W. G., & Dalgarno, A. 1983, ApJ, 264, 485
Draine, B. T., & Woods, D. T. 1990, ApJ, 363, 464
Draine, B. T., & Woods, D. T. 1991, ApJ, 383, 621
Flower, D. R., & Pineau des Forêts, G. 2003, MNRAS, 343, 390
Frail, D. A., Goss, W. M., Reynoso, E. M., et al. 1996, AJ, 111, 1651
Froebrich, D., Davis, C. J., Ioannidis, G., et al. 2011, MNRAS, 413, 480
Fuente, A., Navarro, D. G., Caselli, P., et al. 2019, A&A, 624, A105
Gildas Team 2013, GILDAS: Grenoble Image and Line Data Analysis Software, Astrophysics Source Code Library, ascl:1305.010
Godard, B., Pineau des Forêts, G., Lesaffre, P., et al. 2019, A&A, 622, A100
Goldsmith, P. F., & Langer, W. D. 1978, ApJ, 222, 881
Grassi, T., Bovino, S., Schleicher, D. R. G., et al. 2014, MNRAS, 439, 2386
H.E.S.S. Collaboration, Abdalla, H., Abramowski, A., et al. 2018, A&A, 612, A5
Hily-Blant, P., Faure, A., Rist, C., Pineau des Forêts, G., & Flower, D. R. 2018, MNRAS, 477, 4454
Hinton, J. A., & Hofmann, W. 2009, ARA&A, 47, 523
Holland-Ashford, T., Lopez, L. A., & Auchettl, K. 2020, ApJ, 903, 108
Hwang, U., Petre, R., & Hughes, J. P. 2000, ApJ, 532, 970
Immler, S., & Kuntz, K. D. 2005, ApJL, 632, L99
Indriolo, N., Blake, G. A., Goto, M., et al. 2010, ApJ, 724, 1357

Jiang, B., Chen, Y., Wang, J., et al. 2010, ApJ, 712, 1147
Joye, W. A., & Mandel, E. 2003, in ASP Conf. Ser. 295, Astronomical Data Analysis Software and Systems XII, ed. H. E. Payne, R. I. Jedrzejewski, & R. N. Hook (San Francisco, CA: ASP), 489
Kazes, I. 1970, A&A, 4, 111
Keller, B. W., & Kruijssen, J. M. D. 2022, MNRAS, 512, 199
Keohane, J. W., Reach, W. T., Rho, J., & Jarrett, T. H. 2007, ApJ, 654, 938
Koo, B.-C., Kim, C.-G., Park, S., & Ostriker, E. C. 2020, ApJ, 905, 35
Koo, B.-C., Lee, J.-J., Jeong, I.-G., Seok, J. Y., & Kim, H.-J. 2016, ApJ, 821, 20
Lacey, C. K., Lazio, T. J. W., Kassim, N. E., et al. 2001, ApJ, 559, 954
Lebouteiller, V., Péquignot, D., Cormier, D., et al. 2017, A&A, 602, A45
Lee, Y.-H., Koo, B.-C., & Lee, J.-J. 2020, AJ, 160, 263
Lee, Y.-H., Koo, B.-C., Lee, J.-J., Burton, M. G., & Ryder, S. 2019, AJ, 157, 123
Le Gal, R., Hily-Blant, P., Faure, A., et al. 2014, A&A, 562, A83
Lesaffre, P., Chièze, J. P., Cabrit, S., & Pineau des Forêts, G. 2004, A&A, 427, 157
Lesaffre, P., Pineau des Forêts, G., Godard, B., et al. 2013, A&A, 550, A106
Liu, B., Anderson, L. D., McIntyre, T., et al. 2019, ApJS, 240, 14
Lockhart, I. A., & Goss, W. M. 1978, A&A, 67, 355
Lopez, L. A., Pearson, S., Ramirez-Ruiz, E., et al. 2013a, ApJ, 777, 145
Lopez, L. A., Ramirez-Ruiz, E., Castro, D., & Pearson, S. 2013b, ApJ, 764, 50
Loughnane, R. M., Redman, M. P., Thompson, M. A., et al. 2012, MNRAS, 420, 1367
Lucas, R., & Liszt, H. 1998, A&A, 337, 246
Maloney, P. R., Hollenbach, D. J., & Tielens, A. G. G. M. 1996, ApJ, 466, 561
Mangum, J. G., & Shirley, Y. L. 2015, PASP, 127, 266
Mannheim, K., & Schlickeiser, R. 1994, A&A, 286, 983
McKee, C. F., & Cowie, L. L. 1975, ApJ, 195, 715
Meijerink, R., & Spaans, M. 2005, A&A, 436, 397
Miceli, M., Decourchelle, A., Ballet, J., et al. 2006, A&A, 453, 567
Miettinen, O. 2014, A&A, 562, A3
Ostriker, E. C., & Shetty, R. 2011, ApJ, 731, 41
Ozawa, M., Koyama, K., Yamaguchi, H., Masai, K., & Tamagawa, T. 2009, ApJL, 706, L71
Pety, J. 2005, in SF2A-2005: Semaine de l'Astrophysique Francaise, ed. F. Casoli et al. (Les Ulis: EDP Sciences), 721
Radhakrishnan, V., Goss, W. M., Murray, J. D., & Brooks, J. W. 1972, ApJS, 24, 49
Reach, W. T., Rho, J., Tappe, A., et al. 2006, AJ, 131, 1479
Reid, M. J., Menten, K. M., Brunthaler, A., et al. 2014, ApJ, 783, 130
Sano, H., Yoshiike, S., Yamane, Y., et al. 2021, ApJ, 919, 123
Scannapieco, C., Tissera, P. B., White, S. D. M., & Springel, V. 2008, MNRAS, 389, 1137
Siegel, J., Dwarkadas, V. V., Frank, K. A., & Burrows, D. N. 2020, ApJ, 904, 175
Slane, P., Bykov, A., Ellison, D. C., Dubner, G., & Castro, D. 2015, SSRv, 188, 187
Smithsonian Astrophysical Observatory 2000, SAOImage DS9: A Utility for Displaying Astronomical Images in the X11 Window Environment, Astrophysics Source Code Library, ascl:0003.002
Sun, L., & Chen, Y. 2020, ApJ, 893, 90
Vallini, L., Tielens, A. G. G. M., Pallottini, A., et al. 2019, MNRAS, 490, 4502
van der Tak, F. F. S., & van Dishoeck, E. F. 2000, A&A, 358, L79
Vaupré, S., Hily-Blant, P., Ceccarelli, C., et al. 2014, A&A, 568, A50
Vink, J. 2012, A&ARv, 20, 49
Vink, J. 2020, Physics and Evolution of Supernova Remnants (Cham: Springer)
Walmsley, C. M., Churchwell, E., Nash, A., & Fitzpatrick, E. 1982, ApJL, 258, L75
Wenger, T. V., Balser, D. S., Anderson, L. D., & Bania, T. M. 2018, ApJ, 856, 52
Yamaguchi, H., Tanaka, T., Wik, D. R., et al. 2018, ApJL, 868, L35
Zhang, B., Reid, M. J., Menten, K. M., et al. 2013, ApJ, 775, 79
Zhang, G.-Y., Slavin, J. D., Foster, A., et al. 2019, ApJ, 875, 81
Zhou, P., Li, J.-T., Zhang, Z.-Y., et al. 2018, ApJ, 865, 6
Zhou, P., & Vink, J. 2018, A&A, 615, A150
Zhou, X., Miceli, M., Bocchino, F., Orlando, S., & Chen, Y. 2011, MNRAS, 415, 244
Zhu, H., Tian, W. W., & Zuo, P. 2014, ApJ, 793, 95